

RESEARCH ARTICLE

[View Article Online](#)
[View Journal](#) | [View Issue](#)



Cite this: *Inorg. Chem. Front.*, 2024, **11**, 3744

RbPbPS₄: a promising IR nonlinear optical material achieved by lone-pair-cation-substitution-induced structure transformation†

A-Yang Wang,^{†,a,b,c} Sheng-Hua Zhou,^{†,a,d} Mao-Yin Ran,^{a,b,e} Bingxuan Li,^{a,b} Xin-Tao Wu,^{ID, a,b} Hua Lin^{ID, *a,b} and Qi-Long Zhu^{ID, *a,b}

When stereochemically-active-lone-pair (SCALP) cations are introduced into chalcogenide systems, it is beneficial to produce a remarkable second-harmonic generation (SHG) response (d_{eff}), but it also causes a narrow band gap (E_g), which ultimately results in negative two-photon and free-carrier absorption. Hence, how to obtain a wide E_g (>2.33 eV) while maintaining a strong d_{eff} remains a significant challenge in this domain. In this work, Rb is partially replaced by SCALP Pb in the known ternary centrosymmetric (CS) Rb₃PS₄ (space group: *Pnma*). This results in a quaternary non-centrosymmetric (NCS) RbPbPS₄ (space group: *P2₁2₁2₁*), which possesses distinct 2D [PbPS₄]⁻ layers and Rb⁺ occupies the interlayer spaces as the counter cations. Notably, RbPbPS₄ exhibits a promising overall performance, including strong d_{eff} (2.5 × AgGaS₂), wide IR transmittance cutoff edge (up to 18.1 μm) along with the large E_g (2.75 eV), resulting in an improved laser-induced damage threshold (7.5 × AgGaS₂). Theoretical calculations further indicated that the favorable balance between strong d_{eff} and large E_g in RbPbPS₄ can be attributed to the synergies of the [PbS₇] and [PS₄] nonlinear optical (NLO)-active units. This study not only presents a high-performance Pb-based IR-NLO candidate but also underscores the effectiveness of partial substitution of SCALP cations in inducing a CS-to-NCS structural transformation.

Received 25th April 2024,
Accepted 18th May 2024

DOI: 10.1039/d4qi01040j
rsc.li/frontiers-inorganic

Introduction

Nonlinear optical (NLO) materials have garnered unprecedented attention in laser science and technology because of their ability to facilitate frequency conversion in solid-state laser devices.¹ As widely recognized, an excellent NLO candidate should meet several crucial prerequisites: a sufficient second-harmonic generation (SHG) intensity (d_{eff}), a large energy gap (E_g), a wide optical transparent window, a moderate birefringence (Δn), chemical stability, and availability for

obtaining large single crystals.² In the infrared (IR) region, numerous vital fields, including optoelectronic instruments, resource exploration, and remote laser communication, has sparked widespread attention and interest. Despite the strong d_{eff} exhibited by commercial IR-NLO crystals such as AgGaQ₂ (Q = S, Se)³ and ZnGeP₂,⁴ which make them suitable for applications in the IR region, they still suffer from limitations in high-power laser systems due to their low laser-induced damage thresholds (LIDT) or detrimental two-photon absorption, primarily attributed to their small E_g . However, integrating these optical performances into a single crystal is extremely challenging because they typically depend on competing structural requirements, such as the trade-off between wide E_g and strong d_{eff} .⁵ Therefore, it is of scientific and technological significance to explore new IR-NLO crystals with outstanding comprehensive performance to overcome these challenges.

In addition to the performance prerequisites mentioned above, a prerequisite of an IR-NLO crystal is that it has a non-centrosymmetric (NCS) structure.⁶ The addition of stereochemically-active-lone-pair (SCALP) cations, like As³⁺, Sb³⁺, Bi³⁺, Sn²⁺, and Pb²⁺, to chalcogenide systems has attracted the most attention among all the feasible approaches for creating IR-NLO materials because the majority of these chalcogenides exhibit exceptional IR-NLO performances.⁷ Among these

^aState Key Laboratory of Structural Chemistry, Fujian Institute of Research on the Structure of Matter, Chinese Academy of Sciences, Fuzhou 350002, China.

E-mail: linhua@fjirsm.ac.cn, qlzhu@fjirsm.ac.cn

^bFujian Science & Technology Innovation Laboratory for Optoelectronic Information of China, Fuzhou, Fujian 350108, China

^cCollege of Chemistry, Fuzhou University, Fuzhou 350002, China

^dResource environment & Clean energy Laboratory, School of Chemistry and Chemical Engineering, Jiangsu University of Technology 213001, China

^eUniversity of Chinese Academy of Sciences, Beijing 100049, China

† Electronic supplementary information (ESI) available: Additional experimental and theory results, together with additional tables and figures. CCDC 2347371. For ESI and crystallographic data in CIF or other electronic format see DOI: <https://doi.org/10.1039/d4qi01040j>

‡ A. Y. Wang and S. H. Zhou contributed equally to this work.



cations, Pb^{2+} makes a significant contribution to the d_{eff} but adversely affects the optical E_g .⁸ As is known, narrow energy gaps ($E_g < 2.33$ eV) are unable to mitigate some harmful two-photon or free-carrier absorption under fundamental 1064 nm laser sources.⁹ Therefore, achieving a wide E_g (>2.33 eV) while maintaining a strong d_{eff} remains a significant challenge in Pb-based IR-NLO material design. On the other hand, partial chemical substitution in view of known centrosymmetric (CS) parent structures has shown to be a straightforward but incredibly successful approach in recent years for the design and synthesis of novel high-performance SCALP-based IR-NLO crystals.¹⁰ Successful examples include NCS $\text{Ba}_2\text{As}_2\text{Se}_5$ (parent structure: CS $\text{Ba}_2\text{GaAsSe}_5$),¹¹ NCS $\text{K}_2\text{Ag}_3\text{Sb}_3\text{S}_7$ (parent structure: CS $\text{K}_2\text{Sb}_4\text{S}_7$),¹² NCS ABiP_2S_6 ($\text{A} = \text{K, Rb}$) (parent structure: CS $\text{A}_4\text{P}_2\text{S}_6$),^{13,14} NCS $\text{Sn}_7\text{Br}_{10}\text{S}_2$ (parent structure: CS SnBr_2),¹⁵ $\text{Sr}_{2-x}\text{Pb}_x\text{GeSe}_4$ (parent structure: NCS Sr_2GeSe_4),¹⁶ and NCS Pb_4SeBr_6 (parent structure: CS PbBr_2).¹⁷ Considering these

factors, our focus lies in identifying suitable CS parent structures with wide E_g and achieving CS-to-NCS structural transformation by introducing SCALP Pb for partial chemical substitution. This approach aims to obtain NCS materials with excellent, well-balanced IR-NLO performance.

The ternary chalcophosphate Rb_3PS_4 has piqued our interest due to its CS space group of Pmna and unique zero-dimensional (0D) cluster structure.¹⁸ By incorporating distorted Pb-based motifs, it is possible to disrupt symmetric centers, leading to structural reconstruction and the formation of NCS compounds. Furthermore, Rb_3PS_4 boasts a sufficiently large E_g (>3.5 eV), which can help offset the potential decrease in E_g resulting from the introduction of SCALP Pb^{2+} cations into new compounds. Following this approach, we have designed and synthesized the quaternary Pb-based thiophosphate RbPbPS_4 , featuring a two-dimensional (2D) layered structure composed of $[\text{PbS}_7]$ polyhedra and $[\text{PS}_4]$ tetrahedra.

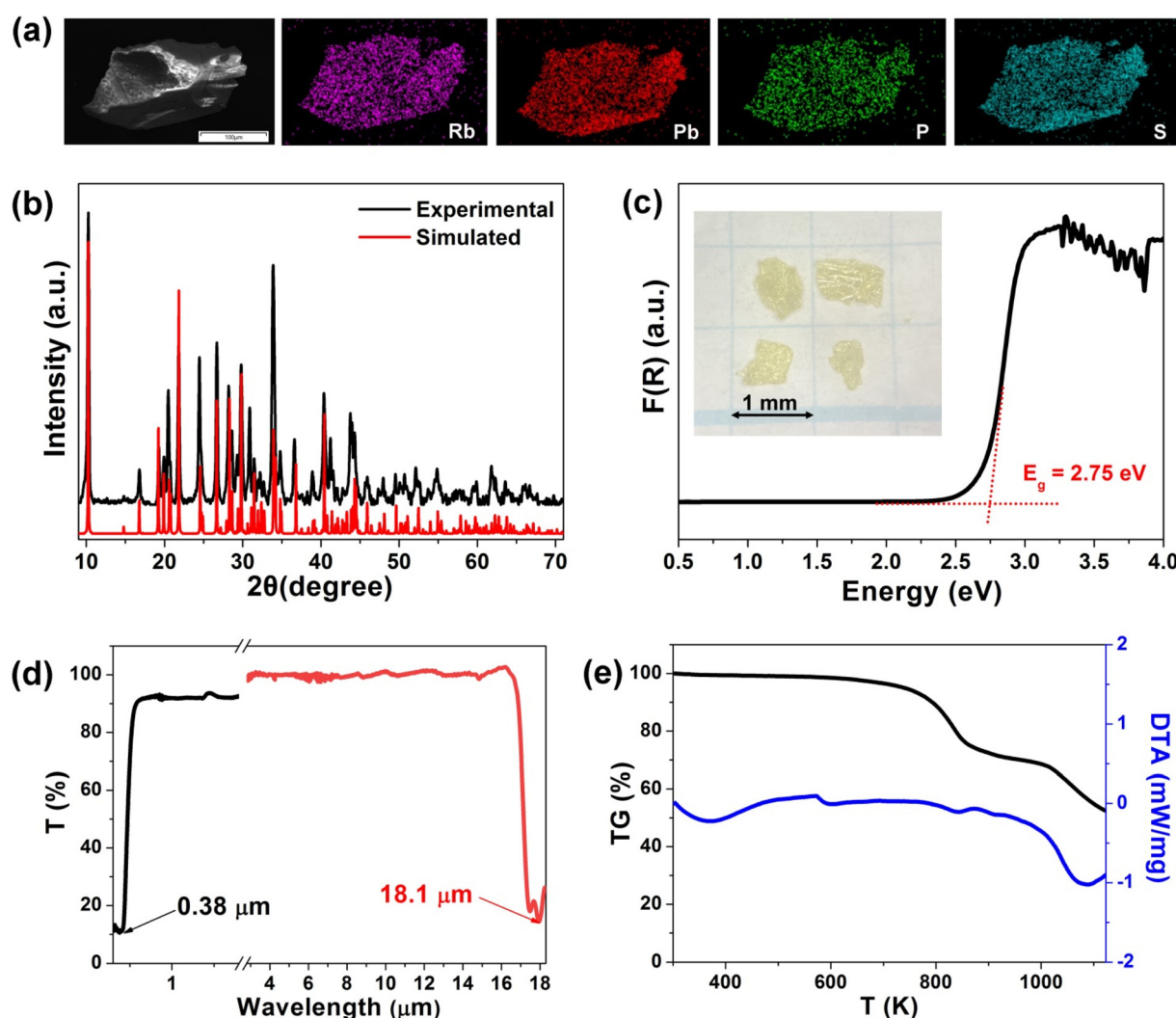


Fig. 1 Experimental characterization results of PbPbPS_4 : (a) SEM image and corresponding elemental distribution maps; (b) experimental (black) and simulated (red) powder XRD patterns; (c) UV-vis-NIR spectrum (inset: photograph of the title crystals); (d) optical transmittance spectrum; (e) TG-DTA test curves.



Remarkably, RbPbPS_4 demonstrates comprehensive IR-NLO performance, including a strong d_{eff} (3.2 times that of AgGaS_2), one of the widest E_g among Pb-based NCS chalcogenides, high LIDT (7.5 times that of AgGaS_2), a broad transmittance range (up to 18.1 μm), and suitable Δn (0.112@2050 nm). In this report, we provide detailed insights into the CS-to-NCS structural transformation and the related optical properties of RbPbPS_4 . Additionally, theoretical calculations are employed to further elucidate its linear optical and NLO performances.

Results and discussion

There are reports of RbPbPS_4 's crystal structure exhibiting two distinct phases.¹⁹ However, we meticulously determined the structure of the title compound to explore the intricate relationship between its NCS crystal structure and NLO properties. Light yellow lamellar crystals of RbPbPS_4 , with sizes reaching the millimeter level, were grown using a simple boron-chalcogen method.²⁰ This method differs from previously reported techniques, which often necessitate complex

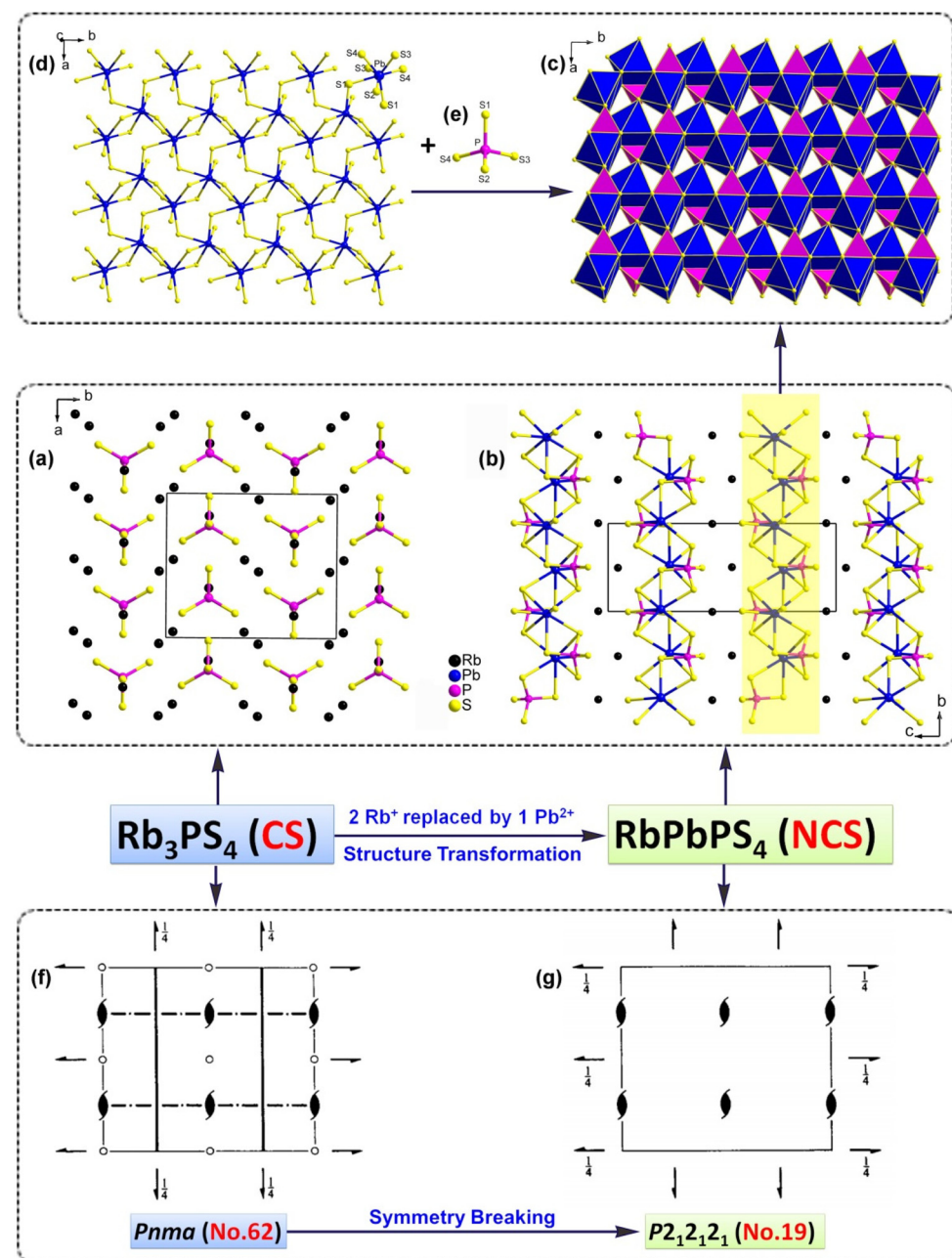


Fig. 2 Structure evolution from ternary CS Rb_3PS_4 to quaternary NCS RbPbPS_4 : view of the 2D layered structures of (a) Rb_3PS_4 and (b) RbPbPS_4 along the ab and bc plane, respectively; (c) a polyhedral 2D layer $[\text{PbPS}_4]^-$ composed of (d) 2D Pb-S layer and (e) discrete tetrahedral $[\text{PS}_4]^-$ motifs; (f) and (g) spatial symmetry operation changing from CS Pnma (no. 62) to NCS $\text{P}2_1\text{2}_1\text{2}_1$ (no. 19).



experimental procedures or involve the use of costly and hazardous elemental Rb as a raw material. Elemental distribution maps indicate that Rb, Pb, P, and S are uniformly distributed throughout the crystals (Fig. 1a). Furthermore, EDX results confirmed that the average molar ratios of the title compound correspond to the formula determined by single-crystal XRD analysis (Fig. S1†). Powder XRD testing validated the phase purity of the title compound, as the experimental patterns closely matched the simulated data obtained from single-crystal XRD analyses (Fig. 1b). The UV-vis diffuse reflectance spectrum of RbPbPS_4 is depicted in Fig. 1c, and absorption data were derived using the Kubelka–Munk equation.²¹ With an experimental optical E_g of 2.75 eV, RbPbPS_4 exhibits the second-highest recorded value among Pb-based IR-NLO chalcogenides. Additionally, RbPbPS_4 demonstrates broad optical transparency across the 0.38–18.1 μm range (Fig. 1d). Thermogravimetric-differential thermal analysis (TG-DTA) was employed to assess the thermal stability of RbPbPS_4 , revealing that the compound remains stable below 700 K (Fig. 1e).

In the asymmetric unit, ternary Rb_3PS_4 has two independent Rb atoms (Wyckoff positions: $4c$ and $8d$), one independent P atom (Wyckoff position: $4c$), and two independent S atoms (Wyckoff positions: $4c$ and $8d$). The P^{5+} cation is located in the center of its common tetrahedron, with P-S bond lengths ranging from 2.043 to 2.055 Å and the bond angles in the range of 108.82 – 111.48 °. Ternary Rb_3PS_4 belongs to the orthorhombic system [space group: $Pnma$ (no. 62)] and the crystal structure consists of counterbalanced Rb^+ cations situated in between discrete tetrahedral $[\text{PS}_4]$ basic building units (BBUs) aligned parallel in opposing orientations (Fig. 2a). Unfortunately, Rb_3PS_4 lacks NLO activity due to its CS crystal structure.

Quaternary RbPbPS_4 adopts the NCS orthorhombic space group $P2_12_12_1$ (no. 19, Table S1†), according to single-crystal XRD investigation. The cell lattice possesses dimensions of $a = 6.3981(2)$ Å, $b = 6.6888(2)$ Å, $c = 17.2823(5)$ Å, and $V = 739.61(4)$ Å³. These crystal parameters are in good agreement with the NCS phase that was previously published. The compound has a 2D layered structure with discrete counterbalanced Rb^+ cations inserted in the channels that are arranged in an “ABABAB” mode perpendicular to the ab -plane (Fig. 2b and c). With seven S atoms polyhedral coordinating each Pb atom in the structure, the highly distorted $[\text{PbS}_7]$ BBUs with Pb–S bond lengths of 2.916–3.281 Å are formed. As shown in Fig. 2d, adjacent $[\text{PbS}_7]$ BBUs are joined by apex-sharing S atoms to generate a 2D Pb–S layer. While the P–S bonds in RbPbPS_4 range in length from 2.031 to 2.069 Å and in bond angles from 106.56° to 111.62°, each P atom is comparable to that of Rb_3PS_4 and is encircled by four S atoms, forming the deformed $[\text{PS}_4]$ tetrahedron (Table S2†). Subsequently, apex-sharing between these 2D Pb–S layers (Fig. 2d) and distinct $[\text{PS}_4]$ BBUs (Fig. 2e) progressively linked them, resulting in the formation of a 2D $[\text{PbPS}_4]^-$ anionic layer (Fig. 2c).

Fig. 2 shows the CS-to-NCS structural evolution *via* partial SCALP cation substitution from ternary CS Rb₃PS₄ to quaternary NCS RbPbPS₄. From a structural perspective, the following

noteworthy modifications have been made following the partial replacement of Rb by SCALP Pb. First off, the initial highly symmetric structure is broken by the addition of SCALP $[PbS_7]$ BBUs and the reassembly of discrete $[PS_4]$ BBUs, which

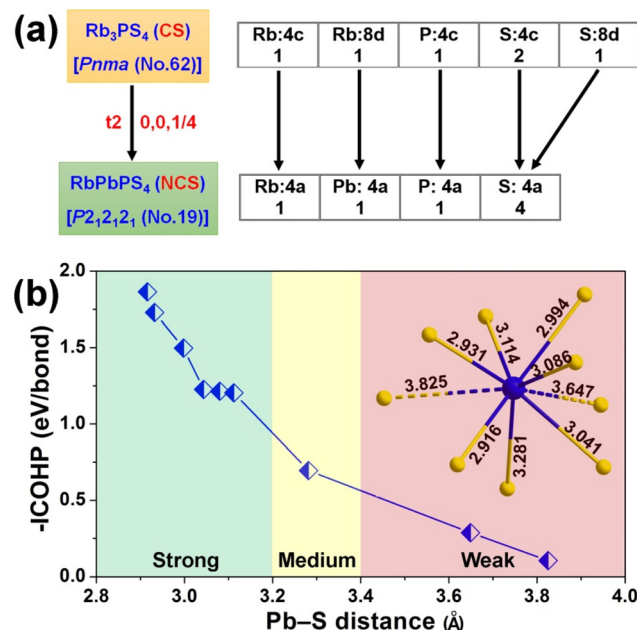


Fig. 3 (a) Group–subgroup relations between CS Rb_3PS_4 [space group: Pmna (no. 62)] and NCS RbPbPS_4 [space group: $\text{P}2_1\text{2}_1\text{2}_1$ (no. 19)]; (b) crystal orbital Hamilton population (COHP) curves for the Pb–S bond length in RbPbPS_4 (the inset figure is the coordination geometry of Pb atom).

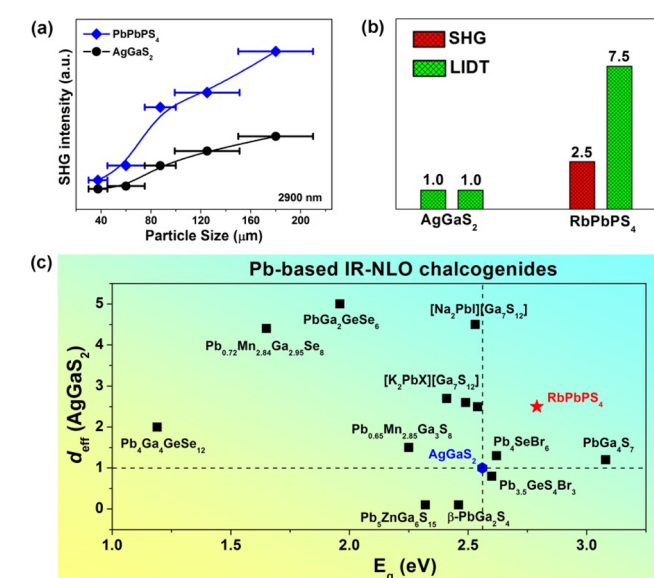


Fig. 4 (a) SHG intensities vs. particle size at $\lambda = 2900$ nm for PbPbPS_4 and AgGaS_2 ; (b) the relative SHG and LIDT intensities of PbPbPS_4 and reference commercial material AgGaS_2 in the particle size of 150–210 μm ; (c) comparison of d_{eff} ($\times\text{AgGaS}_2$) and E_g (eV) of reported Pb-based IR-NLO chalcogenides.

convert the 0D cluster structure into a 2D layered structure. Fig. 2f and g show the detailed symmetric operation modifications that occur after the substitution of SCALP Pb^{2+} cations, resulting in the removal of all center sites and the realization of the CS-to-NCS structural evolution. In particular, space group $Pnma$ (no. 62) converts to $P2_12_12_1$ (no. 19) from the Bärnighausen tree *via* a *translationengleiche* reduction in index 2's symmetry (Fig. 3a).²² When Pb is substituted for Rb, the atomic positions (4c and 8d) in Rb_3PS_4 become 4a in RbPbPS_4 (see Table S3† for details). To put it briefly, the novel compound that was produced, RbPbPS_4 , has good structural anisotropy, which helps to get a higher Δn for achieving PM feature. Secondly, the coordination number (CN) of the two crystallographically independent Rb atoms in Rb_3PS_4 differ (CN = 8 for Rb1 and CN = 9 for Rb2), but are identical in RbPbPS_4 (CN = 11) with Rb-S bond distances less than 4.4 Å (refer to Fig. S2 and S3 in ESI†). Finally, considering the flexible CN of Pb^{2+} cations, the integrated crystal orbital Hamilton population (ICOHP) curve was examined.²³ As depicted in Fig. 3b, it is evident that the short Pb-S bond lengthes of 2.916–3.114 Å exhibit stronger bonding interactions compared

to the long Pb-S bond lengthes (3.647–3.825 Å), while the Pb-S bond distance of 3.281 Å falls between them, representing a medium interaction (see Table S2† for details). Based on the above analysis, it is reasonable to infer that the Pb atom forms a $[\text{PbS}_7]$ mono-capped triangular prism. Research on the distinct $[\text{PbS}_7]$ coordination mode in NCS chalcogenides is notably lacking, and a seven-coordinated example of this has been reported in $\text{Pb}_5\text{Ga}_6\text{ZnS}_{15}$.^{8d} Pb^{2+} cations in NCS chalcogenides are mostly five-coordinated (as in $[\text{Na}_2\text{PbI}][\text{Ga}_7\text{S}_{12}]$ ^{8f}) or six-coordinated (as in $\text{Pb}_4\text{Ga}_4\text{GeS}_{12}$ ^{8a} and $\text{Pb}_{0.65}\text{Mn}_{2.85}\text{Ga}_3\text{S}_8$ ^{8b}), among other compounds that have been found.

Furthermore, through comparison with known ternary and quaternary chalcophosphates, it is determined that substituting SCALP Pb for partial alkali metal Rb is the most optimal and rational structural approach to accomplish the CS-to-NCS structural transformation of template structure Rb_3PS_4 . Fig. S4† provides a detailed structural evolution. Roughly speaking, these replacements fall into three categories. In the first, three Rb atoms are completely substituted by one trivalent element or three monovalent elements in the absence of

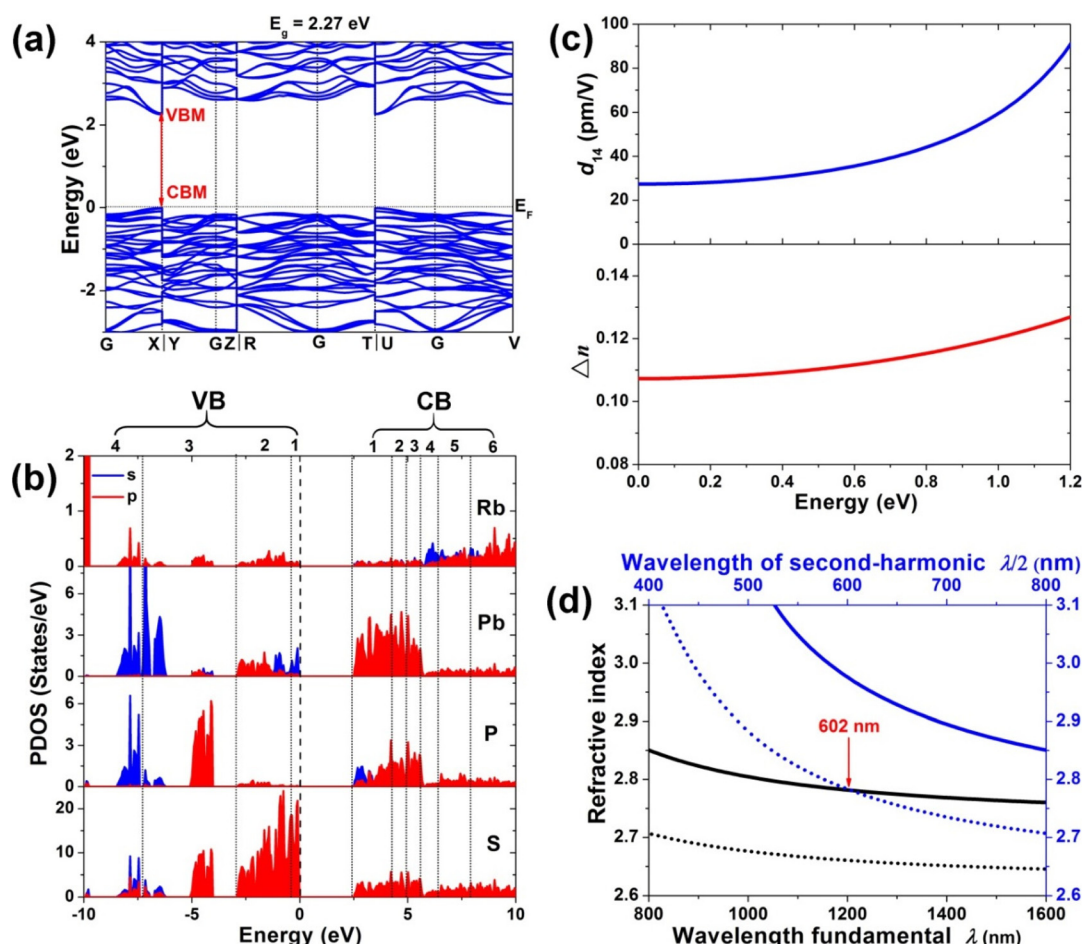


Fig. 5 Theoretical results of electronic structures and optical parameters of PbPbPS_4 : (a) band structure; (b) partial density of states; (c) calculated nonzero independent SHG coefficient d_{14} (pm V^{-1}) and calculated birefringence (Δn); (d) calculated refractive index dispersion curves with the shortest type-I PM cut-off wavelength.



SCALP components. CS structures are displayed by the resultant compounds, including REPS_4 (space group: $I4_1/acd$),²⁴ BPS_4 (space group: $Ibam$),²⁵ GaPS_4 (space group: $P2_1/c$),²⁶ and Ti_3PS_4 (space group: $Pnma$).²⁷ The second category entails complete substitution of SCALP elements, as seen in SbPS_4 (space group: $P\bar{1}$)²⁸ and BiPS_4 (space group: $Ibca$),²⁹ which also belong to the CS structures. The third category involves partial substitution, where Rb is partially replaced by monovalent or divalent elements. The resulting compounds, such as Rb_2AgPS_4 (space group: $P\bar{1}$),³⁰ $\text{RbAg}_5\text{P}_2\text{S}_8$ (space group: $Pbca$),³¹ RbSrPS_4 (space group: $Pnma$),³² RbBaPS_4 (space group: $Pnma$),³³ RbPdPS_4 (space group: $I4/mcm$),³⁴ and RbHgPS_4 (space group: $P2_1/n$),³⁵ all adopt CS structures. Therefore, it is reasonable to replace partial Rb with SCALP elements to realize a structural transition from CS Rb_3PS_4 to NCS RbPbPS_4 . Hence, employing established CS chalcophosphates as the parent structure and partially substituting them with SCALP-cation groups proves to be an effective chemical strategy for accomplishing the CS-to-NCS structural evolution.

As RbPbPS_4 belongs to the NCS space group $P2_12_12_1$ and possesses the NLO-active motifs $[\text{PbS}_7]$ and $[\text{PS}_4]$, a relatively

strong d_{eff} could be expected. Powder SHG testing for RbPbPS_4 was conducted using the modified Kurtz–Perry technology,³⁵ with irradiation from a 2900 nm laser and commercial material AgGaS_2 as a reference. As depicted in Fig. 4a, the positive correlation between the particle size and SHG intensity indicates that RbPbPS_4 exhibits PM behavior. The SHG intensity of RbPbPS_4 is approximately 2.5 times that of benchmark AgGaS_2 in a particle size range of 150–210 μm (Fig. 4b). Based on $d_{\text{eff}} = d_{\text{eff},\text{R}} (I^2\omega/I_{\text{R}}^2\omega)^{1/2}$ ($d_{\text{eff},\text{R}} = 13.4 \text{ pm V}^{-1}$ for AgGaS_2), the effective SHG coefficient d_{eff} of RbPbPS_4 at 2900 nm is 21.2 pm V^{-1} . In addition, powder LIDT measurement was employed to preliminarily evaluate the LIDT value,³⁶ with the increased optical E_g suggesting that the title crystal would exhibit higher LIDT. As illustrated in Fig. 4b, the LIDT of RbPbPS_4 (10.88 MW cm^{-2}) is estimated to be 7.5 times that of AgGaS_2 (1.45 MW cm^{-2}) under the same testing conditions. Compared with other reported Pb-based IR-NLO materials (Fig. 4c and Table S4†), RbPbPS_4 demonstrates a favorable balance between strong d_{eff} and large E_g . Notably, RbPbPS_4 represents the first quaternary Pb-based chalcogenide to overcome the incompatibility between a wide E_g ($>2.56 \text{ eV}$, the E_g of AgGaS_2) and a

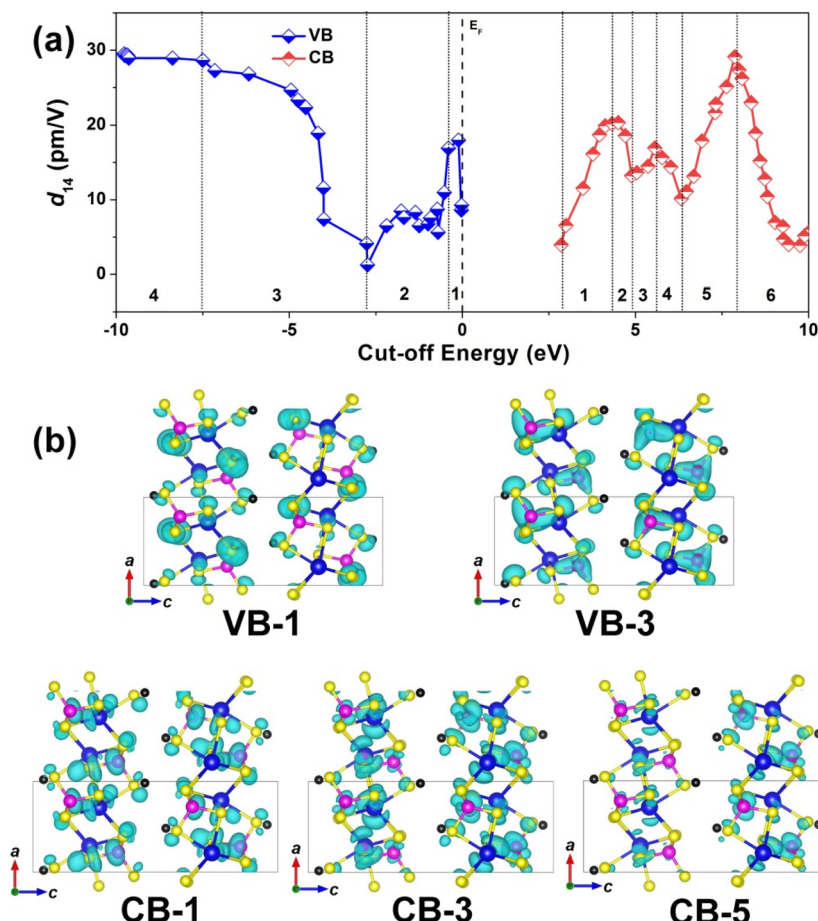


Fig. 6 Theoretical analysis of the intrinsic mechanism of SHG source for PbPbPS_4 : (a) cut-off energy (eV) dependence of the static d_{14} (pm V^{-1}); (b) distribution of the partial charge density maps with major contributions in the VB-1, VB-3, CB-1, CB-3 and CB-5 regions. Black atoms: Rb; blue atoms: Pb; pink atoms: P; yellow atoms: S.



sufficient d_{eff} ($>1.0 \times \text{AgGaS}_2$). This balance IR-NLO performance can be compared to the recently reported quaternary NCS chalcogenides, such as $\alpha\text{-Li}_2\text{ZnGeS}_4$,³⁷ $\text{Li}_4\text{CdSn}_2\text{S}_7$,³⁸ $\text{NaMg}_3\text{Ga}_3\text{S}_8$,³⁹ and $(\text{CuI})_3\text{P}_4\text{S}_4$.⁴⁰

To gain further insights into the underlying structure–property relationship of the title compound, systematic theoretical calculations were conducted, encompassing band structure, densities of states (DOSSs), and linear optical and NLO parameters, based on DFT. The calculated electronic band structure reveals a direct E_g of 2.27 eV for RbPbPS_4 , as the valence band maximum (VBM) and conduction band minimum (CBM) coincide at the same high-symmetry k -points (Fig. 5a). The smaller calculated E_g can be attributed to underestimation by the DFT calculation.⁴¹ The partial DOSSs of RbPbPS_4 are depicted in Fig. 5b, indicating that the tops of the VBs are predominantly composed of S-3p states, with a minor contribution from Pb-5s and P-3p states, while the bottoms of the CBs primarily consist of S-3p, Pb-5p, P-3s/3p, and Rb-5p states. Furthermore, the NLO coefficients of RbPbPS_4 can be calculated according to the electronic structure. In the light of Kleinman symmetry,⁴² RbPbPS_4 exhibits only one nonzero independent SHG coefficient, $d_{14} = 31.8 \text{ pm V}^{-1}$ at 2900 nm (*ca.* 0.43 eV) (Fig. 5c). Furthermore, the calculated d_{eff} of RbPbPS_4 is 26.88 pm V^{-1} , under 2900 nm irradiation,³⁵ which essentially coincides with the experimental findings. Additionally, the calculated Δn value of RbPbPS_4 is 0.109 at 2900 nm, significantly surpassing that of AgGaS_2 ($\Delta n \sim 0.04$).⁴³ This suggests that RbPbPS_4 may be well-suited to achieve the PM condition for the SHG process. Furthermore, the line refractive dispersion diagrams indicate that the shortest type-I phase-matched output wavelength is 602 nm (Fig. 5d).⁴⁴

To visually illustrate the contribution of the constituent BBUs to the SHG effect, the cutoff energy dependence of the static d_{14} for RbPbPS_4 is calculated using a length-gauge formalism method.⁴⁵ As depicted in Fig. 6a, the d_{14} values exhibit an upward trend in the VB-1, VB-3, CB-1, CB-3, and CB-5 intervals. This illustrates that the orbitals in these regions have a significant influence on the overall NLO response.⁴⁶ Moreover, by integrating the partial DOSSs (Fig. 5b) with the relevant partial charge density maps (Fig. 6b), it is evident that the enhancement of the d_{eff} in RbPbPS_4 primarily stems from the strong hybridization of electron states at the top of the VBs and the substantial distortion of $[\text{PbS}_7]$ and $[\text{PS}_4]$ groups, indicative of the 2D $[\text{PbPS}_4]^-$ alternating arrangement layer.

Conclusions

In summary, building upon the parent ternary CS compound Rb_3PS_4 , we implemented a strategy involving the partial substitution of Rb with SCALP Pb, resulting in the creation of a new quaternary NCS chalcophosphate, RbPbPS_4 . This substitution also triggered a structural transformation from 0D clusters to 2D layers. As anticipated, experimental findings highlight RbPbPS_4 as a promising candidate for IR-NLO applications, boasting a large d_{eff} ($2.5 \times \text{AgGaS}_2$ at 2900 nm), a broad trans-

mittance cutoff window (0.38–18.1 μm), and a significant E_g (2.75 eV) conducive to a high LIDT ($7.5 \times \text{AgGaS}_2$ at 1064 nm). Detailed structure–property analyses elucidate that the strong calculated d_{eff} (26.88 pm V^{-1} at 2900 nm) and large calculated birefringence (0.109@2900 nm) in RbPbPS_4 primarily stem from the cooperative effects of $[\text{PbS}_7]$ and $[\text{PS}_4]$ NLO-active motifs. These findings underscore the efficacy of the lone-pair participation substitution strategy in achieving both structural transformation and effectively balancing strong d_{eff} with a large E_g in SCALP-based chalcogenides.

Author contributions

A-Yang Wang: investigation, formal analysis, writing – original draft. Sheng-Hua Zhou: investigation, methodology, validation. Mao-Yin Ran: investigation, formal analysis, validation. Bingxuan Li: formal analysis, validation. Xin-Tao Wu: conceptualization, writing – review & editing. Hua Lin: supervision, conceptualization, writing – review & editing. Qi-Long Zhu: supervision, writing – review & editing.

Conflicts of interest

There are no conflicts to declare.

Acknowledgements

This work was supported by the National Natural Science Foundation of China (22175175), Natural Science Foundation of Fujian Province (2022L3092 and 2023H0041), Fujian Science & Technology Innovation Laboratory for Optoelectronic Information of China (2021ZR118), and the Youth Innovation Promotion Association CAS (2022303). The authors thank Prof. Yong-Fan Zhang at Fuzhou University for helping with the DFT calculations.

References

- (a) F. J. Duarte, *Tunable Laser Applications*, CRC Press, Boca Raton, FL, 2008, ch. 2, 9 and 12; (b) V. Petrov, Frequency down-conversion of solid-state laser sources to the mid-infrared spectral range using non-oxide nonlinear crystals, *Prog. Quantum Electron.*, 2015, **44**, 1–106; (c) X.-T. Wu and L. Chen, Structure-Property Relationships in Nonlinear Optical Crystals II The IR Region, *Structure Bonding*, 2012, **145**, 1–42; (d) N. L. B. Sayson, T. Bi, V. Ng, H. Pham, L. S. Trainor, H. G. L. Schwefel, S. Coen, M. Erkintalo and S. G. Murdoch, Octave-spanning tunable parametric oscillation in crystalline Kerr microresonators, *Nat. Photonics*, 2019, **13**, 701–706; (e) J.-X. Zhang, P. Feng, M.-Y. Ran, X.-T. Wu, H. Lin and Q.-L. Zhu, Ga-based IR nonlinear optical materials: Synthesis, structures, and properties, *Coord. Chem. Rev.*, 2024, **502**, 215617.



2 (a) L. Kang, M. Zhou, J. Yao, Z. Lin, Y. Wu and C. Chen, Metal Thiophosphates with Good Mid-infrared Nonlinear Optical Performances: A First-Principles Prediction and Analysis, *J. Am. Chem. Soc.*, 2015, **137**, 13049–13059; (b) P. S. Halasyamani and W. Zhang, Viewpoint: Inorganic Materials for UV and Deep-UV Nonlinear-Optical Applications, *Inorg. Chem.*, 2017, **56**, 12077–12085; (c) Y. Pan, S.-P. Guo, B.-W. Liu, H.-G. Xue and G.-C. Guo, Second-order nonlinear optical crystals with mixed anions, *Coord. Chem. Rev.*, 2018, **374**, 464–496; (d) M. Mutailipu, K. R. Poeppelmeier and S. Pan, Borates: A Rich Source for Optical Materials, *Chem. Rev.*, 2021, **121**, 1130–1202; (e) H. Chen, M.-Y. Ran, W.-B. Wei, X.-T. Wu, H. Lin and Q.-L. Zhu, A comprehensive review on metal chalcogenides with three-dimensional frameworks for infrared nonlinear optical applications, *Coord. Chem. Rev.*, 2022, **470**, 214706.

3 (a) A. Harasaki and K. J. Kato, New Data on the Nonlinear Optical Constant, Phase-Matching, and Optical Damage of AgGaS_2 , *Appl. Phys.*, 1997, **36**, 700–703; (b) G. C. Catella, L. R. Shiozawa, J. R. Hietanen, R. C. Eckardt, R. K. Route, R. S. Feigelson, D. G. Cooper and C. L. Marquardt, Mid-IR absorption in AgGaSe_2 optical parametric oscillator crystals, *Appl. Opt.*, 1993, **32**, 3948–3951.

4 G. D. Boyd, E. Buehler and F. G. Storz, Linear and nonlinear optical properties of ZnGeP_2 and CdSe , *Appl. Phys. Lett.*, 1971, **18**, 301–304.

5 (a) K. Wu and S. Pan, A review on structure-performance relationship toward the optimal design of infrared nonlinear optical materials with balanced performances, *Coord. Chem. Rev.*, 2018, **377**, 191–208; (b) L. Kang, F. Liang, X. Jiang, Z. Lin and C. Chen, First-Principles Design and Simulations Promote the Development of Nonlinear Optical Crystals, *Acc. Chem. Res.*, 2020, **53**, 209–217; (c) W. Wang, D. Mei, F. Liang, J. Zhao, Y. Wu and Z. Lin, Inherent laws between tetrahedral arrangement pattern and optical performance in tetrahedron-based mid-infrared nonlinear optical materials, *Coord. Chem. Rev.*, 2020, **421**, 213444; (d) H.-D. Yang, M.-Y. Ran, W.-B. Wei, X.-T. Wu, H. Lin and Q.-L. Zhu, Recent advances in IR nonlinear optical chalcogenides with well-balanced comprehensive performance, *Mater. Today Phys.*, 2023, **35**, 101127; (e) L. Luo, L. Wang, J. Chen, J. Zhou, Z. Yang, S. Pan and J. Li, $\text{AlB}_3\text{IIC}_3\text{IIIQ}_8\text{VI}$: A New Family for the Design of Infrared Nonlinear Optical Materials by Coupling Octahedra and Tetrahedra Units, *J. Am. Chem. Soc.*, 2022, **144**, 21916–21925; (f) M.-Y. Ran, S.-H. Zhou, W.-B. Wei, B.-X. Li, X.-T. Wu, H. Lin and Q.-L. Zhu, Breaking through the Trade-Off between Wide Band Gap and Large SHG Coefficient in Mercury-based Chalcogenides for IR Nonlinear Optical Application, *Small*, 2024, **20**, 2304563; (g) W. Zhou and S.-P. Guo, Rational Design of Novel Promising Infrared Nonlinear Optical Materials: Structural Chemistry and Balanced Performances, *Acc. Chem. Res.*, 2024, **57**, 648–660.

6 (a) P. S. Halasyamani and K. R. Poeppelmeier, Noncentrosymmetric Oxides, *Chem. Mater.*, 1998, **10**, 2753–2769; (b) K. M. Ok, Toward the Rational Design of Novel Noncentrosymmetric Materials: Factors Influencing the Framework Structures, *Acc. Chem. Res.*, 2016, **49**, 2774–2785; (c) Y. Hu, C. Wu, X. Jiang, Z. Wang, Z. Huang, Z. Lin, X. Long, M. G. Humphrey and C. Zhang, Giant Second-Harmonic Generation Response and Large Band Gap in the Partially Fluorinated Mid-Infrared Oxide $\text{RbTeMo}_2\text{O}_8\text{F}$, *J. Am. Chem. Soc.*, 2021, **143**, 12455–12459; (d) H. Chen, W.-B. Wei, H. Lin and X.-T. Wu, Transition-metal-based chalcogenides: A rich source of infrared nonlinear optical materials, *Coord. Chem. Rev.*, 2021, **448**, 214154; (e) P.-F. Li, J.-G. Mao and F. Kong, A survey of stereoactive oxysalts for linear and nonlinear optical applications, *Mater. Today Phys.*, 2023, **37**, 101197.

7 (a) M. Yan, H.-G. Xue and S.-P. Guo, Recent Achievements in Lone-Pair Cation-Based Infrared Second-Order Nonlinear Optical Materials, *Cryst. Growth Des.*, 2021, **21**, 698–720; (b) T. K. Bera, J.-H. Song, A. J. Freeman, J. I. Jang, J. B. Ketterson and M. G. Kanatzidis, Soluble direct-band-gap semiconductors LiAsS_2 and NaAsS_2 : Large electronic structure effects from weak As center dot center dot center dot S interactions and strong nonlinear optical response, *Angew. Chem., Int. Ed.*, 2008, **47**, 7828–7832; (c) F. Xu, X. Xu, B. Li, G. Zhang, C. Zheng, J. Chen and N. Ye, $\text{Hg}_3\text{As}_4\text{X}$ (X = Cl and Br): two Hg-based chalcogenides as long-wave infrared nonlinear optical crystals with superior comprehensive performances, *Inorg. Chem. Front.*, 2024, **11**, 2105–2115; (d) H. Lin, Y. Y. Li, M. Y. Li, Z. J. Ma, L. M. Wu, X. T. Wu and Q. L. Zhu, Centric-to-acentric structure transformation induced by a stereochemically active lone pair: a new insight for design of IR nonlinear optical materials, *J. Mater. Chem. C*, 2019, **7**, 4638–4643; (e) Y. Xiao, M. M. Chen, Y. Y. Shen, P. F. Liu, H. Lin and Y. Liu, $\text{A}_3\text{Mn}_2\text{Sb}_3\text{S}_8$ (A = K, Rb): A new type of multifunctional infrared nonlinear optical materials based on unique three-dimensional open frameworks, *Inorg. Chem. Front.*, 2021, **8**, 2835–2843; (f) H.-J. Zhao, H.-D. Yang, P.-F. Liu and H. Lin, From Cc to P6₃mc: Structural Variation in $\text{La}_3\text{S}_2\text{Cl}_2[\text{SbS}_3]$ and $\text{La}_3\text{OSCl}_2[\text{SbS}_3]$ Induced by the Isovalent Anion Substitution, *Cryst. Growth Des.*, 2022, **22**, 1437–1444; (g) Y. Zhou, L.-T. Jiang, X.-M. Jiang, B.-W. Liu and G.-C. Guo, Mixed-anion square-pyramid $[\text{SbS}_3\text{I}_2]$ units causing strong second-harmonic generation intensity and large birefringence, *Chin. Chem. Lett.*, 2024, 109740; (h) M. Y. Li, B. X. Li, H. Lin, Z. J. Ma, L. M. Wu, X. T. Wu and Q. L. Zhu, $\text{Sn}_2\text{Ga}_2\text{S}_5$: A Polar Semiconductor with Exceptional Infrared Nonlinear Optical Properties Originating from the Combined Effect of Mixed Asymmetric Building Motifs, *Chem. Mater.*, 2019, **31**, 6268–6275; (i) C. Zhao, B. Zhang, X. Tian, G. Zhou, J. Xu and K. Wu, $\text{Na}_6\text{Sn}_3\text{P}_4\text{S}_{16}$: Sn(II)-chelated PS_4 groups inspired an ultra-strong SHG response, *Inorg. Chem. Front.*, 2023, **10**, 5726–5733; (j) X. Chen, Q. Jing and K. M. Ok, $\text{Pb}_{18}\text{O}_8\text{Cl}_{15}\text{I}_5$: A Polar Lead Mixed Oxyhalide with Unprecedented Architecture and Excellent Infrared Nonlinear Optical Properties, *Angew. Chem., Int. Ed.*, 2020, **59**, 20323–20327.



8 (a) Y. K. Chen, M. C. Chen, L. J. Zhou, L. Chen and L. M. Wu, Syntheses, Structures, and Nonlinear Optical Properties of Quaternary Chalcogenides: $Pb_4Ga_4GeQ_{12}$ (Q = S, Se), *Inorg. Chem.*, 2013, **52**, 8334–8341; (b) M. Zhou, X. Jiang, Y. Guo, Z. Lin, J. Yao and Y. Wu, $Pb_{0.65}Mn_{2.85}Ga_3S_8$ and $Pb_{0.72}Mn_{2.84}Ga_{2.95}Se_8$: Two Quaternary Metal Chalcognides with Open-Tunnel-Framework Structures Displaying Intense Second Harmonic Generation Responses and Interesting Magnetic Properties, *Inorg. Chem.*, 2017, **56**, 8454–8461; (c) Z. Z. Luo, C. S. Lin, H. H. Cui, W. L. Zhang, H. Zhang, H. Chen, Z. Z. He and W. D. Cheng, $PbGa_2MSe_6$ (M = Si, Ge): Two Exceptional Infrared Nonlinear Optical Crystals, *Chem. Mater.*, 2015, **27**, 914–922; (d) R. H. Duan, J. S. Yu, H. Lin, Y. J. Zheng, H. J. Zhao, S. X. Huang-Fu, M. A. Khan, L. Chen and L. M. Wu, $Pb_5Ga_6ZnS_{15}$: a noncentrosymmetric framework with chains of T_2 -supertetrahedra, *Dalton Trans.*, 2016, **45**, 12288–12291; (e) W. F. Chen, B. W. Liu, X. M. Jiang and G. C. Guo, Infrared nonlinear optical performances of a new sulfide β - $PbGa_2S_4$, *J. Alloys Compd.*, 2022, **905**, 164090; (f) Z. X. Wu, W. F. Chen, X. M. Jiang, B. W. Liu and G. C. Guo, $[Na_2PbI][Ga_7S_{12}]$: Combining Diamond-Like Anionic Framework with Polycationic Chain toward Achieving Remarkable Nonlinear Optical Response, *Chem. Mater.*, 2024, **36**, 3444–3451; (g) W. F. Chen, B. W. Liu, S. M. Pei, X. M. Jiang and G. C. Guo, $[K_2PbX][Ga_7S_{12}]$ (X = Cl, Br, I): The First Lead-Containing Cationic Moieties with Ultrahigh Second-Harmonic Generation and Band Gaps Exceeding the Criterion of 2.33 eV, *Adv. Sci.*, 2023, **10**, 2207630; (h) J. Zhou, H. Wang, J. Liu, X. Su, Y. Chu, J. Qu and X. Jiang, $Pb_{3.5}GeS_4Br_3$: The first phase-matching thiogerminate halide infrared nonlinear optical material, *Inorg. Chem. Front.*, 2024, **11**, 2681–2689; (i) J. Wang, H. Wu, H. Yu, Z. Hu, J. Wang and Y. Wu, Pb_4SeBr_6 : A Congruently Melting Mid-Infrared Nonlinear Optical Material with Excellent Comprehensive Performance, *Adv. Opt. Mater.*, 2022, **10**, 2102673; (j) X. Li, L. Kang, C. Li, Z. Lin, J. Yao and Y. Wu, $PbGa_4S_7$: a wide-gap nonlinear optical material, *J. Mater. Chem. C*, 2015, **3**, 3060–3067.

9 J. Chen, Q. Wu, H. Tian, X. Jiang, F. Xu, X. Zhao, Z. Lin, M. Luo and N. Ye, Uncovering a Vital Band Gap Mechanism of Pnictides, *Adv. Sci.*, 2022, **9**, 2105787.

10 (a) H. Lin, W. B. Wei, H. Chen, X. T. Wu and Q. L. Zhu, Rational design of infrared nonlinear optical chalcogenides by chemical substitution, *Coord. Chem. Rev.*, 2020, **406**, 213150; (b) M.-Y. Ran, A. Y. Wang, W. B. Wei, X.-T. Wu, H. Lin and Q.-L. Zhu, Recent progress in the design of IR nonlinear optical materials by partial chemical substitution: Structural evolution and performance optimization, *Coord. Chem. Rev.*, 2023, **481**, 215059.

11 M.-M. Chen, Z. Ma, B.-X. Li, W.-B. Wei, X.-T. Wu, H. Lin and Q.-L. Zhu, $M_2As_2Q_5$ (M = Ba, Pb Q = S, Se): A source of infrared nonlinear optical materials with excellent overall performance activated by multiple discrete arsenate anions, *J. Mater. Chem. C*, 2021, **9**, 1156–1163.

12 C. Liu, S.-H. Zhou, Y. Xiao, C. Zhang, H. Lin and Y. Liu, Aliovalent-cation-substitution-induced structure transformation: a new path toward high-performance IR nonlinear optical materials, *J. Mater. Chem. C*, 2021, **9**, 15407–15414.

13 M. M. Chen, S. H. Zhou, W. B. Wei, B. X. Li, M. Y. Ran, X. T. Wu, H. Lin and Q. L. Zhu, $RbBiP_2S_6$: A Promising IR Nonlinear Optical Material with a Giant Second-Harmonic Generation Response Designed by Aliovalent Substitution, *ACS Mater. Lett.*, 2022, **4**, 1264–1269.

14 V. Nguyen, B. Ji, K. Wu, B. Zhang and J. Wang, Unprecedented mid-infrared nonlinear optical materials achieved by crystal structure engineering, a case study of $(KX)P_2S_6$ (X = Sb, Bi, Ba), *Chem. Sci.*, 2022, **13**, 2640–2648.

15 X. H. Li, Z. H. Shi, M. Yang, W. Liu and S. P. Guo, $Sn_3Br_{10}S_2$: The First Ternary Halogen-Rich Chalcohalide Exhibiting a Chiral Structure and Pronounced Nonlinear Optical Properties, *Angew. Chem., Int. Ed.*, 2022, **61**, e202115871.

16 L. T. Menezes, A. Assoud, W. Zhang, P. S. Halasyamani and H. Kleinke, Effect of Pb Substitution in $Sr_{(2-x)}Pb_xGeSe_4$ on Crystal Structures and Nonlinear Optical Properties Predicted by DFT Calculations, *Inorg. Chem.*, 2020, **59**, 15028–15035.

17 J. Wang, H. Wu, H. Yu, Z. Hu, J. Wang and Y. Wu, Pb_4SeBr_6 : A Congruently Melting Mid-Infrared Nonlinear Optical Material with Excellent Comprehensive Performance, *Adv. Opt. Mater.*, 2022, **10**, 2102673.

18 L.-B. Wu and F.-Q. Huang, Crystal structure of trirubidium tetrathiophosphate, Rb_3PS_4 , *Z. Kristallogr. – New Cryst. Struct.*, 2005, **220**, 122–122.

19 (a) J. Yao and J. A. Ibers, $RbPbPS_4$, *Acta Crystallogr., Sect. E: Struct. Rep. Online*, 2004, **60**, i108–i110; (b) I. Belkyl, M. ElAzhari, Y. D. Wu, W. Bensch and W. Depmeier, Phase transition of rubidium lead tetrathiophosphate $RbPbPS_4$, *Z. Anorg. Allg. Chem.*, 2009, **635**, 1600–1603.

20 Y. Z. Huang, L. Chen and L. M. Wu, Submicrosized Rods, Cables, and Tubes of ZnE (E = S, Se, Te): Exterior–Interior Boron-Chalcogen Conversions and Optical Properties, *Inorg. Chem.*, 2008, **47**, 10723–10728.

21 P. Kubelka and F. Munk, Reflection characteristics of paints, *Z. Tech. Phys.*, 1931, **12**, 593–601.

22 U. Englert, *Symmetry Relationships between Crystal Structures*, Oxford University Press: Oxford, UK, 2013.

23 R. Dronskowski and P. E. Bloechl, Crystal orbital Hamilton populations (COHP): energy-resolved visualization of chemical bonding in solids based on density-functional calculations, *J. Phys. Chem.*, 1993, **97**, 8617–8624.

24 T. Komm, D. Gudat and T. Schleid, Die Lanthanid (III)-ortho-Thiophosphate(V) vom Typ $M[PS_4](M = La–Nd, Sm, Gd–Er)$: Synthese, Kristallstruktur und ^{31}P -NMR-Untersuchungen, *Z. Naturforsch.*, 2006, **61b**, 766–774.

25 F. Pielnhofer, L. M. Schoop, A. Kuhn, R. Eger, J. Nuss, H. Nuss and B. V. Lotsch, New Light on an Old Story: The Crystal Structure of Boron Tetrathiophosphate Revisited, *Z. Anorg. Allg. Chem.*, 2019, **645**, 267–271.

26 P. Buck and C. D. Carpentier, The Crystal Structure of Gallium Thiophosphate, $GaPS_4$, *Acta Crystallogr., Sect. B: Struct. Crystallogr. Cryst. Chem.*, 1973, **29**, 1864–1868.

27 P. Toffoli, P. Khodadad and N. Rodier, Structure cristalline du tetrathiomonophosphate (V) de thallium(I) Tl_3PS_4 , *Bull. Soc. Chim. Fr.*, 1981, 429–432.

28 C. D. Malliakas and M. G. Kanatzidis, Inorganic Single Wall Nanotubes of $SbPS_{4-x}Se_x$ ($0 \leq x \leq 3$) with Tunable Band Gap, *J. Am. Chem. Soc.*, 2006, **128**, 6538–6539.

29 D. Tiwari, D. Alibhai, D. Cherns and D. J. Fermin, Crystal and Electronic Structure of Bismuth Thiophosphate, $BiPS_4$: An Earth-Abundant Solar Absorber, *Chem. Mater.*, 2020, **32**, 1235–1242.

30 F. Alahmari, B. Davaasuren, J. Khanderi and A. Rothenberger, Synthesis and Characterization of the Rubidium Thiophosphate $Rb_6(PS_5)(P_2S_{10})$ and the Rubidium Silver Thiophosphates Rb_2AgPS_4 , $RbAg_5(PS_4)_2$ and $Rb_3Ag_9(PS_4)_4$, *Z. Anorg. Allg. Chem.*, 2016, **642**, 361–367.

31 A. Mesbah, J. Prakash, D. Rocca, S. Lebègue, J. C. Beard, B. A. Lewis and J. A. Ibers, Syntheses, crystal structure, and electronic properties of the five $ABaMQ_4$ compounds $RbBaPS_4$, $CsBaPS_4$, $CsBaVS_4$, $RbBaVSe_4$, and $CsBaVSe_4$, *J. Solid State Chem.*, 2016, **233**, 217–220.

32 Y. Huang, J. Huang and Y. Zhang, Wide band gap thiophosphates $ASrPS_4$ ($A = Li, Na, K, Rb, Cs$): cation size effect induced successive structural transformation, *Dalton Trans.*, 2022, **51**, 15067–15073.

33 S. Coste, J. Hanko, M. Bujoli-Doeuff, G. Louarn, M. Evain, R. Brec, B. Alonso, S. Jobic and M. G. Kanatzidis, $NaPdPS_4$ and $RbPdPS_4$: systems with infinite straight $\frac{1}{\infty} [PdPS_4]^-$ chains soluble in polar solvents and the structure of cubic $RbPdPS_4\{Rb_{0.33}P_{0.4}S_{2.23}O_x\}$, *J. Solid State Chem.*, 2003, **175**, 133–145.

34 W. Xing, C. Tang, P. Gong, J. Wu, Z. Lin, J. Yao, W. Yin and B. Kang, Investigation into Structural Variation from 3D to 1D and Strong Second Harmonic Generation of the $AHgPS_4$ ($A^+ = Na^+, K^+, Rb^+, Cs^+$) Family, *Inorg. Chem.*, 2021, **60**, 18370–18378.

35 S. K. Kurtz and T. T. Perry, A powder technique for the evaluation of nonlinear optical materials, *J. Appl. Phys.*, 1968, **39**, 3798–3813.

36 M. J. Zhang, X. M. Jiang, L. J. Zhou and G. C. Guo, Two phases of Ga_2S_3 : promising infrared second-order nonlinear optical materials with very high laser induced damage thresholds, *J. Mater. Chem. C*, 2013, **1**, 4754–4760.

37 J.-H. Zhang, D. J. Clark, J. A. Brant, K. A. Rosmus, P. Grima, J. W. Lekse, J. I. Jang and J. A. Aitken, α - Li_2ZnGeS_4 : A Wide-Bandgap Diamond-like Semiconductor with Excellent Balance between Laser-Induced Damage Threshold and Second Harmonic Generation Response, *Chem. Mater.*, 2020, **32**, 8947–8955.

38 J.-H. Zhang, S. S. Stoyko, A. J. Craig, P. Grima, J. W. Kotchey, J. I. Jang and J. A. Aitken, Phase Matching, Strong Frequency Doubling, and Outstanding Laser-Induced Damage Threshold in the Biaxial, Quaternary Diamond-like Semiconductor $Li_4CdSn_2S_7$, *Chem. Mater.*, 2020, **32**, 10045–10054.

39 L. Luo, L. Wang, J. Chen, J. Zhou, Z. Yang, S. Pan and J. Li, $A^I B^{II}_3 C^{III}_3 Q^{VI}_8$: A New Family for the Design of Infrared Nonlinear Optical Materials by Coupling Octahedra and Tetrahedra Units, *J. Am. Chem. Soc.*, 2022, **144**, 21916–21925.

40 S. Yang, C. Lin, H. Fan, K. Chen, G. Zhang, N. Ye and M. Luo, Polar Phosphorus Chalcogenide Cage Molecules: Enhancement of Nonlinear Optical Properties in Adducts, *Angew. Chem., Int. Ed.*, 2023, **62**, e202218272.

41 K. Burke, Perspective on density functional theory, *J. Chem. Phys.*, 2012, **136**, 150901.

42 D. A. Kleinman, Nonlinear Dielectric Polarization in Optical Media, *Phys. Rev.*, 1962, **126**, 1977–1979.

43 (a) M. Y. Li, Z. J. Ma, B. X. Li, X. T. Wu, H. Lin and Q. L. Zhu, $HgCuPS_4$: An Exceptional Infrared Nonlinear Optical Material with Defect Diamond-like Structure, *Chem. Mater.*, 2020, **32**, 4331–4339; (b) M. Y. Ran, Z. J. Ma, H. Chen, B. X. Li, X. T. Wu, H. Lin and Q. L. Zhu, Partial Isovalent Anion Substitution to Access Remarkable Second-Harmonic Generation Response: A Generic and Effective Strategy for Design of Infrared Nonlinear Optical Materials, *Chem. Mater.*, 2020, **32**, 5890–5896; (c) M. M. Chen, S. H. Zhou, W. B. Wei, X. T. Wu, H. Lin and Q. L. Zhu, Phase Matchability Transformation in the Infrared Nonlinear Optical Materials with Diamond-Like Frameworks, *Adv. Opt. Mater.*, 2022, **10**, 2102123.

44 (a) M. Y. Ran, S. H. Zhou, B. X. Li, W. B. Wei, X. T. Wu, H. Lin and Q. L. Zhu, Enhanced Second-Harmonic-Generation Efficiency and Birefringence in Melillite Oxychalcogenides $Sr_2MGe_2OS_6$ ($M = Mn, Zn, and Cd$), *Chem. Mater.*, 2022, **34**, 3853–3861; (b) A.-Y. Wang, S. H. Zhou, M. Y. Ran, X. T. Wu, H. Lin and Q. L. Zhu, Regulating the key performance parameters for Hg -based IR NLO chalcogenides via bandgap engineering strategy, *Chin. Chem. Lett.*, 2024, **35**, 109377; (c) M. Y. Ran, S. H. Zhou, X. T. Wu, H. Lin and Q. L. Zhu, The first Hg -based oxychalcogenide $Sr_2HgGe_2OS_6$: Achieving balanced IR nonlinear optical properties through synergistic cation and anion substitution, *Mater. Today Phys.*, 2024, **44**, 101442.

45 (a) C. Aversa and J. E. Sipe, Nonlinear optical susceptibilities of semiconductors: Results with a length-gauge analysis, *Phys. Rev. B: Condens. Matter Mater. Phys.*, 1995, **52**, 14636–14645; (b) S. N. Rashkeev, W. R. L. Lambrecht and B. Segall, Efficient ab initio method for the calculation of frequency-dependent second-order optical response in semiconductors, *Phys. Rev. B: Condens. Matter Mater. Phys.*, 1998, **57**, 3905–3919.

46 (a) H. Chen, Y.-Y. Li, B.-X. Li, P.-F. Liu, H. Lin, Q.-L. Zhu and X.-T. Wu, Salt-Inclusion Chalcogenide $[Ba_4Cl_2][ZnGa_4S_{10}]$: Rational Design of an IR Nonlinear Optical Material with Superior Comprehensive Performance Derived from $AgGaS_2$, *Chem. Mater.*, 2020, **32**, 8012–8019; (b) H.-D. Yang, M.-Y. Ran, S.-H. Zhou, B.-X. Li, X.-T. Wu, H. Lin and Q.-L. Zhu, Rational Design via Dual-Site Aliovalent Substitution Leads to an Outstanding IR Nonlinear Optical Material with Well-Balanced Comprehensive Properties, *Chem. Sci.*, 2022, **13**, 10725–10733; (c) M.-Y. Ran, S.-H. Zhou, W.-B. Wei, B.-X. Li,



X.-T. Wu, H. Lin and Q.-L. Zhu, Rational Design of a Rare-Earth Oxychalcogenide $\text{Nd}_3[\text{Ga}_3\text{O}_3\text{S}_3][\text{Ge}_2\text{O}_7]$ with Superior Infrared Nonlinear Optical Performance, *Small*, 2023, **19**, 2300248; (d) H. Chen, M.-Y. Ran, S.-H. Zhou, X.-T. Wu,

H. Lin and Q.-L. Zhu, Simple yet extraordinary: super-polyhedra-built 3D chalcogenide framework of $\text{Cs}_5\text{Ga}_9\text{S}_{16}$ with excellent infrared nonlinear optical performance, *Chin. Chem. Lett.*, 2023, **34**, 107838.

